ACS APPLIED OPTICAL MATERIALS

pubs.acs.org/acsaom Article

Twist-Driven Deep-Ultraviolet-Wavelength Exciton Funnel Effect in Bilayer Boron Nitride

Linghan Zhu, Yizhou Wang, and Li Yang*

Cite This: ACS Appl. Opt. Mater. 2024, 2, 166−172 Read Online

ACCESS | Metrics & More | Article Recommendations | Supporting Information

ABSTRACT: Realizing direct band gap quantum dots working within the deep-ultraviolet frequency is highly desired for electro-optical and biomedical applications while remaining challenging. In this work, we combine first-principles many-body perturbation theory and effective Hamiltonian approximation to propose the realization of arrays of deep-ultraviolet excitonic quantum dots in twisted bilayer hexagonal boron nitride. The effective quantum confinement of excitons can reach ∼400 meV within small twisting angles, which is about four times larger than those observed in twisted semiconducting transition metal dichalcogenides. Especially because of enhanced electron−hole attraction, those excitons will accumulate via the so-called exciton funnel effect to the direct band gap regime, giving the possibility to better luminescence performance and manipulating coherent arrays of deep-ultraviolet quantum dots.

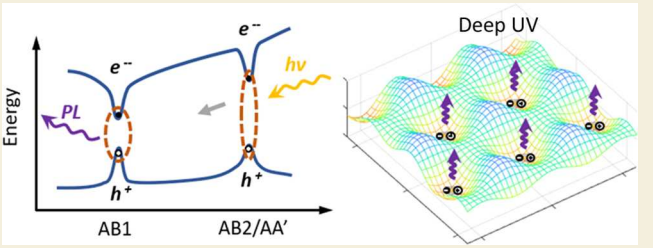

KEYWORDS: *excitonic quantum dot arrays, moiré superlattices, bilayer BN, exciton funnel effect, GW-BSE calculations*

INTRODUCTION

Quantum dots (QDs), also known as "artificial atoms", have been widely utilized as fundamental building blocks in various applications, including light emitters/detectors,[1,2] photovoltaics,[3] biomedical sensors,[4] and photo/electrocatalysis.[5,6] Recent advancements in twisted two-dimensional (2D) van der Waals (vdW) bilayers have opened up new possibilities for creating arrays of QDs with uniform sizes.[7,8] The formation of moiré superlattices in these systems, with periodic potential landscapes spanning hundreds or thousands of unit cells, naturally creates quantum wells for carrier confinement. Twisted transition metal dichalcogenide (TMD) heterostructures have particularly been demonstrated to hold promise in realizing a variety of quantum emitters with high purity.[9−12] However, most intrinsic few-layer TMDs are indirect band gap semiconductors, limiting their optical quantum yield and efficiency.[13] To overcome this limitation, heterostructures with a type II band alignment have been employed to create few-layer systems with direct band gaps.[12,14] Electronically doped TMD moiré heterostructures have been shown to exhibit Mott insulating states and generalized Wigner crystals with atomic-like orbitals.[15−18] Excitonic quantum emitter arrays are proposed in twisted TMD bilayers under an electric field.[8] Nonetheless, the moiré confinement potential induced in these TMD systems is typically less than 100 meV,[7−9,19,20] making their optical performance and correlated properties temperature-sensitive, and the increased material complexity and required external fields further limit their broader applications.

Despite significant advancements in twist-driven TMD QDs operating in the infrared/visible frequency, there have been limited proposals to extend their functionality into the deep-ultraviolet (DUV) regime, covering wavelengths from 280 nm down to 200 nm. The DUV domain is crucial for broad applications, including polymer curing,[21] air−water purification,[22] biomedical instrumentation,[23] quantum sensing,[24] and germicidal systems.[25] Layered hexagonal boron nitride (*h*-BN) presents itself as an attractive candidate due to its ultrawide band gap (UWBG) (∼6.2 eV in the bulk structure).[26−28] However, intrinsic few-layer and bulk *h*-BN exhibit indirect band gaps,[26] resulting in the quenching of photoluminescence and limitation of their potential for optical applications.

In this work, we employed first-principles simulations to propose twist-induced DUV QD arrays. We show that by twisting bilayer *h*-BN structures, one can realize QDs with a significant periodic potential confinement of ∼400 meV. Importantly, the minimum band gap within the *h*-BN superlattice is switched to be direct, giving hope to realizing arrays of DUV QDs with an improved quantum yield for optical responses. Going beyond single-particle descriptions, we further incorporate excitonic effects via many-body

Received: October 29, 2023
Revised: December 4, 2023
Accepted: December 6, 2023
Published: December 27, 2023

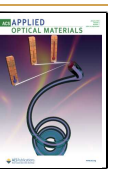

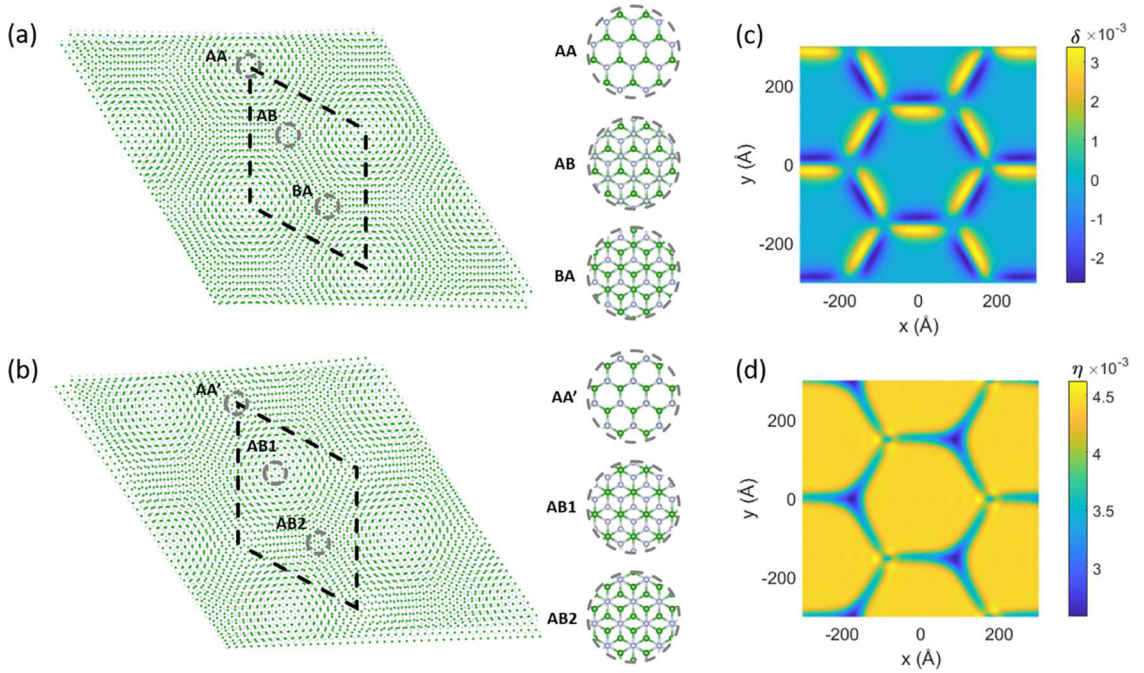

Figure 1. Moiré superlattices formed by a twist from (a) AA and (b) AA′ stacked bilayer *h*-BN. The top views of the atomic structure of local high-symmetry stackings are shown in the circles. (c) The relative local bond length change δ and (d) atomic displacement η in a fully relaxed 0.5° twisted bilayer *h*-BN.

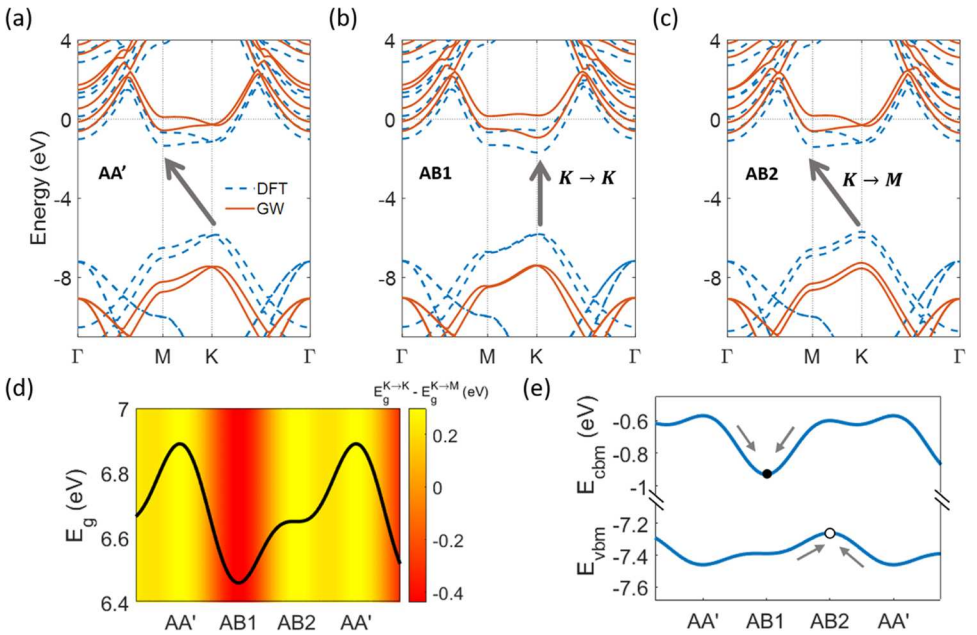

Figure 2. DFT (dashed blue line) and GW (solid red line) band structures of (a) AA′, (b) AB1, and (c) AB2 bilayer *h*-BN stackings. The zero energy is set to the vacuum level. (d) The plane-wave interpolated band gap landscape in the twisted AA′ bilayer *h*-BN moiré superlattice. The background color bar represents the energy difference between the direct gap at *K* and the indirect gap from *K* to *M*. Notice that the deep color represents the region of direct band gaps. (e) The plane-wave interpolated GW-calculated VBM and CBM energies across the high-symmetry stackings in the moiré superlattice. All VBM are at *K*. CBM for AB1 is at *K*, while for AA′ and AB2, those are at *M*.

perturbation theory (MBPT) and explore an exciton funnel effect, wherein the large moiré exciton binding drives photoexcited electron−hole pairs toward the potential minimum dominated by direct excitons. This exciton funnel effect helps concentrate excitons for energy harvesting and enables coherent optical responses of periodic DUV QDs in an intrinsic moiré superlattice.

RESULTS AND DISCUSSION

There are two fundamental stacking orders in *h*-BN. Natural bulk *h*-BN takes the AA′ stacking, where there is a 180° rotation between adjacent layers.[26,29] Two BN monolayer sheets can also be stacked without rotation, realizing the other AA stacking. A small twist between bilayer *h*-BN gives rise to the moiré superlattices, where there is a local variation of

https://doi.org/10.1021/acsaom.3c00389
ACS Appl. Opt. Mater. 2024, 2, 166−172

interlayer stackings within the supercell. Figure 1a,b shows the moiré superlattices formed by twisting AA and AA′ stacked bilayer *h*-BN, respectively. For the twisted AA stacking, two local stackings, AB and BA, are equivalent in the sense that they are related by a spatial inversion. For the twisted AA′ stacking, three distinct high-symmetry stackings AA′, AB1, and AB2 can be identified. Recent theoretical and experimental studies have demonstrated intrinsic ferroelectricity in twisted AA *h*-BN homobilayers since AB and BA configurations break the inversion symmetry.[30−32] On the other hand, all three stackings of the twisted AA′ bilayer keep the inversion symmetry, and no ferroelectricity is expected. In this work, we mainly focus on the twisted bilayer *h*-BN based on the intrinsic AA′ stacking. However, the twist-induced direct band gap and exciton funnel effect proposed in this paper could also be applied to other moiré superlattices.

Lattice reconstruction is considered to be an important issue in the study of twisted vdW materials.[33,34] We have employed LAMMPS[35] to study the local strain introduced by moiré superlattices in twisted bilayer *h*-BN. We adopted the modified Kolmogorov and Crespi (KC) potential[36] to simulate the interlayer interactions and the Tersoff potential[37] for the intralayer interactions. The relative change in local bond length δ and atomic displacement η is defined by

$$\delta = \frac{\Sigma_{i,j} d_{ij} - 3d_{\mathrm{BN}}}{3d_{\mathrm{BN}}} \tag{1}$$

$$\eta = \frac{|\Sigma_{i,j} \vec{d}_{ij}|}{3d_{\mathrm{BN}}} \tag{2}$$

where the summations are over the nearest neighbors and d is the bond length. d_{BN} is the intrinsic bond length. As shown in Figure 1c,d, the local change of bond length and atomic displacement is generally below 0.5% for both metrics in a 0.5° twisted homobilayer *h*-BN. This is expected to affect the electronic structures at the level of ∼10 meV,[38] which will have little impact on the UWBG *h*-BN. Moreover, previous works have shown that the lattice reconstruction-induced strain is inversely proportional to the twist angle.[39] Hence, in the remainder of the paper, we will not consider the strain effect in the interpolation of local band energies for relevant twisting angles between 0.5 and 2°.

Stacking-Dependent Quasiparticle Band Gap

We begin our discussions of the electronic structures of three high-symmetry stackings in a twisted AA′ bilayer with the density functional theory (DFT) results. The electronic band structures of AA′, AB1, and AB2 stacked bilayer *h*-BN are shown in Figure 2a−c, respectively. The DFT results are represented by blue dashed lines. The distinct interlayer atomic configurations of different stackings result in substantially different band structures. Intrinsic AA′ and AB2 stackings take an indirect band gap, where the valence band maximum (VBM) is at *K* and the conduction band minimum (CBM) lies at *M*. In contrast, the AB1 stacking has a direct band gap at *K*. These findings agree with previous works on the electronic structure of bilayer BN.[40,41] The distinction in band structures can be understood from the atomic arrangements of different stackings. In the AB1 stacking, boron atoms in the top layer are vertically aligned with boron atoms in the bottom layer. From the projected density of states (PDOS) of the AB1 stacked bilayer BN [see the Supporting Information[42]], the CBM is mainly contributed by the p orbitals of boron atoms. As a result, the strong interlayer interaction and orbital hybridization lead to a large splitting of the CBM at *K*, resulting in a direct band gap. Similarly, in the AB2 stacking, nitride atoms in the top layer lie above the nitride atoms of the bottom layer. As the VBM of bilayer BN is mainly composed of the p orbital of nitride atoms, this renders the splitting of the VBM in the AB2 stacking.

Since DFT is known to underestimate band gaps of semiconductors and insulators, we further performed the GW approximation to obtain the quasiparticle energies. As shown by the red solid lines in Figure 2a−c, the GW correction does not alter the band alignment but mainly renormalizes the band energies. The direct band gap in the AB1 stacking is enlarged by ∼2.33 eV, and the indirect band gaps in AA′ and AB2 stackings are enlarged by ∼2.37 eV. The self-energy corrections are similar in all three stackings since they are mainly determined by the dimensionality and subsequently reduced electronic screening. The DFT and GW-calculated direct and indirect band gaps are summarized in Table 1.

Table 1. DFT/GW Band Gaps and Exciton Energies for Three High-Symmetry Local Stackings[a]

	$E_{g,K\to K}^{DFT}$ (direct)	$E_{g,K\to M}^{DFT}$ (indirect)	$E_{g,K\to K}^{GW}$ (direct)	$E_{g,K\to M}^{GW}$ (indirect)	E_x^d (direct)	E_x^i (indirect)
AA′	4.74	4.52	7.19	6.89	5.30	5.38
AB1	**4.13**	4.51	**6.46**	6.90	**4.94**	5.45
AB2	4.52	4.29	6.96	6.65	5.18	5.21

[a]The lower-energy values of each stacking are underscored. The global energy minima are in bold font. The energy unit is in eV.

Twist-Driven Continuous Band Gap Variation

We adopt the effective Hamiltonian to obtain the quasiparticle moiré potential in the twisted bilayer *h*-BN superlattices. The periodic quasiparticle band gap variation in moiré superlattices can be approximated by a Fourier expansion over the nearest moiré reciprocal lattice vectors[43] and it is plotted in Figure 2d along the three high-symmetry local stackings. The fitting parameters (T_0, V_0, ψ) from ab initio GW calculations for the band gap are (6.67 eV, 41 meV, 26°) for this C_3 symmetry system. The overall variation of quasiparticle band gap within the moiré superlattice is ∼430 meV, which is significantly larger than those realized in twisted TMDs. Moreover, as demonstrated by the background color in Figure 2d, the region around the moiré potential minimum at the AB1 stacking assumes the direct band gap, which gives hope in realizing high-quantum-yield QD arrays in twisted bilayer *h*-BN. We notice that previous works on strained monolayer TMDs[44−46] can realize similar energy barriers under indirect band gaps. However, by exploiting the natural band gap variation in twisted homobilayers, we bypassed the requirement of strain engineering of ultrastrength materials, making our approach more feasible to realize in experiments.

$$V(\boldsymbol{r}) = E(\boldsymbol{r}) = T_0 + 2V_0\Sigma_{i=1,2,3}\cos(\boldsymbol{b}_i\cdot\boldsymbol{r} \pm \psi) \tag{3}$$

Nonetheless, the photoexcited carrier dynamics and, particularly, luminescence are not only decided by the band gap. Within the single-particle picture, photoexcited carriers in the superlattice tend to move toward the band extrema, as elucidated in Figure 2e, by the gray arrows for electrons (CBM) and holes (VBM), respectively. Interestingly, although the AB1 stacking has the minimum band gap, its VBM is lower

https://doi.org/10.1021/acsaom.3c00389
ACS Appl. Opt. Mater. 2024, 2, 166−172

than that nearby AB2 stacking because of the significant VBM splitting at K point of the AB2 stacking (Figure 2c). As a result, a charge-transfer picture is expected within the single-particle picture, in which excited electrons are accumulated in AB1 stacking, while excited holes are accumulated in AB2 stacking. Such a spatial separation of electrons and holes will diminish optical radiative recombination because of the small overlap between their wave functions, which leads to quenched dipole oscillator strength. Fortunately, in the following, we show that the strong electron−hole interactions and exciton funnel effect in twisted bilayer BN may overcome the spatial separation of electrons and holes and enhance the luminescence intensity.

Exciton Funnel Effect in *h*-BN Moiré Superlattices

It is widely recognized that the optical responses of 2D semiconductors and insulators are dictated by excitonic effects, which are dramatically increased due to reduced dielectric screening.[13,49] For this consideration, we have further solved BSE and calculated excitonic effects in the three high-symmetry stackings, the optical absorption spectra of which are shown in Figure 3a−c. Due to the reduced dimensionality

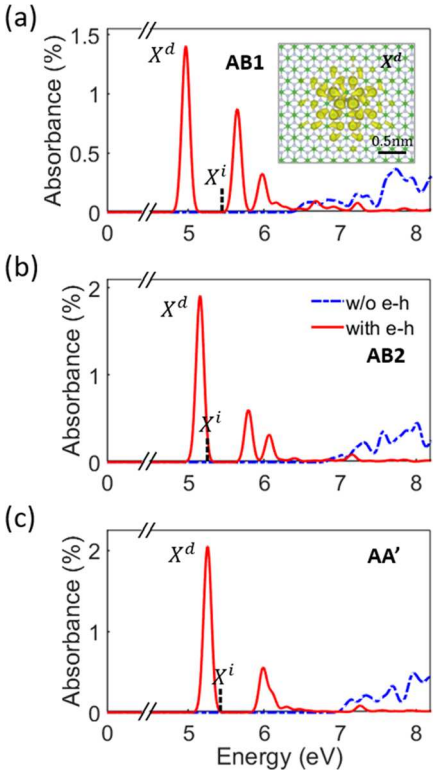

Figure 3. Optical absorption spectra of (a) AA′, (b) AB1, and (c) AB2 stacked bilayer *h*-BN without (blue dashed line) and with (solid red line) electron−hole interactions included. The direct X^d and indirect X^i states are labeled in the plot. The inset in panel (a) represents the real-space exciton wave function of X^d. The hole position is marked with a gray circle.

and dielectric screening, enhanced electron−hole interactions dominate the optical absorption spectra. For the AB1 stacking, the lowest-energy exciton state is a direct exciton X^d located at 4.94 eV with a 1.5 eV of electron−hole binding energy. It is mainly formed by optical transitions from holes to electrons around K in reciprocal space. We also find that around 500 meV above X^d, there is an indirect exciton X^i featuring transitions mainly from K to M with a finite momentum. Because of the requirement of momentum conservation for vertical transitions, indirect exciton X^i is an optically dark state.

Interestingly, for the indirect band gap stackings AA′ and AB2, the lowest-energy exciton state is essentially still a direct exciton, X^d originated from transitions around the K point with a zero momentum, as marked in Figure 3b,c, respectively. This is because the strength of electron−hole interactions is proportional to the electronic structure joint density of states (JDOS).[47] The excitonic transition matrix elements are a coherent sum of the contributing electron−hole pair transitions, which can also be written as an integral in the energy space[48,49]

$$\langle 0|\hat{v}|i\rangle = \sum_{vck} A^{i}_{vck}\langle vk|\hat{v}|ck\rangle = \int S_i(\omega)\mathrm{d}\omega \tag{4}$$

where $S_i(\omega) = \sum_{vck} A^{i}_{vck}\langle vk|\hat{v}|ck\rangle\delta(\omega - (E_{ck} - E_{vk}))$ is essentially the electron−hole coupling coefficient modulated JDOS. This also agrees with the picture of the hydrogenic model, in which a larger effective mass contributes to a larger JDOS and electron−hole binding energy.

As shown in Figure 2a,c, the CBM at K is doubly degenerate for these two stacking styles while they are split at the CBM (M point), which indicates much higher JDOS around K than that at M. The enhanced electron−hole interaction induces a large binding energy, which pushes the zero-momentum (direct) exciton state X^d to a lower energy than that of the indirect exciton state X^i. The lower-energy direct exciton in indirect band gap bilayer *h*-BN has been discovered in a previous theoretical study.[50] The direct and indirect exciton energies of different stackings are summarized in Table 1. The direct X^d exciton binding energy in bilayer BN is large, reaching over 1.5 eV in AB1 and ∼1.8 eV in AA′ and AB2. Although the JDOS and electron−hole binding energy are smaller in the AB1 stacking than in the other two indirect gap stackings, its quasiparticle band gap is the smallest, which leads to its lowest-energy bright X^d state among three high-symmetry sites.

The typical real-space wave functions of the excitonic state X^d are plotted in the inset of Figure 3a. Compared with monolayer TMD, in which the typical exciton size is ∼2.6 nm,[9,51] the exciton radius of bilayer *h*-BN is significantly smaller (∼0.7 nm) because of the weaker screening and stronger electron−hole binding. In twisted bilayer *h*-BN, if we take a twist angle of 1°, the moiré lattice constant is ∼14 nm. The radius of the exciton is much smaller than the superlattice; hence, we can adopt eq 1 and treat the lowest-energy exciton as a composite particle moving within a slowly varying excitonic moiré potential. The moiré potential of exciton energies along the high-symmetry line is plotted in Figure 4a, and all those excitonic states are direct (zero momentum). The variation of direct exciton energy within the moiré period is ∼400 meV, which is comparable to that reported in strain-engineered monolayer MoS_2 under a high strain level (∼500 meV at a biaxial strain of 5%)[44] and much larger than that in twisted bilayer TMDs (∼100 meV).[7,9,52]

Importantly, because the exciton binding energy (∼1.5−1.8 eV) is much larger than the quasiparticle energy variation (∼300 meV), the photoexcited carriers tend to form electron−hole pairs because of the larger energy gain, and their motion is dictated by the energy landscape of excitons, instead of that of single particles shown in Figure 2e. A schematic plot of the electron−hole interaction modified band edge landscape is

https://doi.org/10.1021/acsaom.3c00389
ACS Appl. Opt. Mater. 2024, 2, 166−172

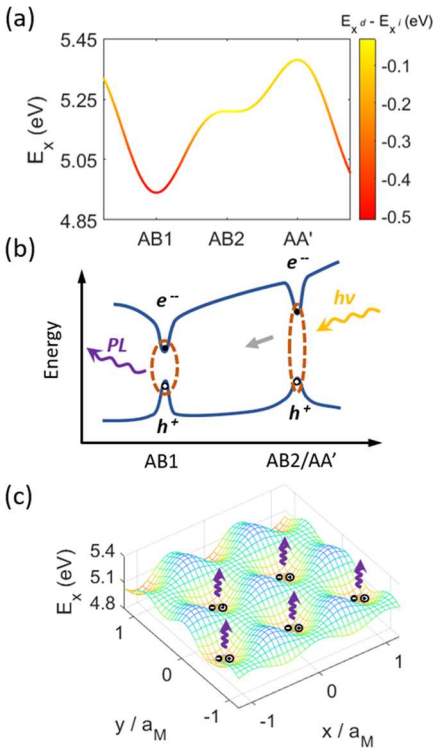

Figure 4. (a) Exciton energy profile in the moiré superlattice. The color bar represents the energy difference between direct X^d and indirect X^i excitons at local stackings. (b) Schematic plot of the modified band edge landscape under photoexcitation due to the electron−hole binding effect. The large exciton binding results in exciton funneling to AB1. The gray arrow shows the motion of excited carriers under incident light. (c) Exciton energy profile in the moiré superlattice, in which the photoexcited excitons are accumulated around the minimum-excitonic-energy region round AB1.

shown in Figure 4b. While the electrons in conduction bands still tend to move toward the overall CBM around the AB1 stacking, the strong exciton binding drags holes in the valence band toward AB1, instead of the overall VBM around AB2. This is essentially the type III exciton funnel effect as proposed previously[44,60] and is a direct result of the overwhelming electron−hole interaction. Therefore, despite the different localizations of VBM and CBM, photoexcited charge carriers (both holes and electrons) will form excitons and accumulate around AB1 stacking in favor of the decreasing exciton energy profile via the exciton funnel effect.

Figure 4c summarizes the exciton energy profile in the moiré superlattice. Because of the accumulation of carriers at the lowest-energy exciton state, excitons will be localized around the AB1 high-symmetry sites. The increased local exciton density will further enhance the intensity of the coherent photoluminescence. Therefore, by exploiting the periodic quasiparticle band gap variation and exciton funnel effect in moiré superlattices of bilayer *h*-BN, we can realize arrays of DUV QDs formed by bright exciton states. Finally, it is worth mentioning that the exciton diffusion length reported in 2D materials is typically on the order of ∼1 μm,[53,54] which is much larger than the moiré period discussed in this work. This validates the proposed exciton funnel effect in the moiré superlattices before the excitons recombine.

Experimental realizations of quantum emitter arrays in strain textured monolayers MoS_2[55] and WSe_2[56] were reported previously by utilizing indented nanopillars, confirming the theoretical predictions of exciton funnel effect in a strain-engineered continuously varying band gap landscape. Besides, we note that recently, there are experimental efforts in realizing the quantum-dot light emitters in MoS_2/WSe_2 heterostructures,[57] and in hexagonal[58] and orthorhombic[59] boron nitride crystals, via the formation of defect states. Our work provides another general and intrinsic approach for achieving excitonic quantum dot arrays in moiré superlattices, which can be verified by photoluminescent measurements on twist-stacked exfoliated monolayer BN.

CONCLUSIONS

By exploiting the large band gap variation in twisted bilayer *h*-BN, we propose the realization of bright DUV QDs in the moiré superlattice with the help of the exciton funnel effect. Through many-body perturbation theory calculations, we show that the large quasiparticle band gap and exciton energy confinement within the moiré structure are significant (∼400 meV). Although the CBM and VBM are located in different high-symmetry areas of the moiré superlattice, the large electron−hole binding energy drives both holes and electrons toward the AB1 stacking to form bright direct[55]excitons owing to the exciton funnel effect. The DUV wavelength excitonic QD arrays could have broad applications in energy harvesting and photolithography.

COMPUTATIONAL DETAILS

The ground-state properties of bilayer *h*-BN are calculated by DFT within the general gradient approximation (GGA) with the Perdew−Burke−Ernzerhof (PBE) exchange−correlation functional[60] as implemented in Quantum ESPRESSO.[61] The vdW interactions are included via the semiempirical Grimme-D3 scheme.[62] The plane-wave energy cutoff is set to 65 Ry under the norm-conserving pseudopotentials. The vacuum level of 18 Å is chosen between adjacent BN bilayers along the out-of-plane direction to avoid spurious interactions. MBPT simulations are performed with BerkeleyGW.[63] The quasiparticle energies are calculated under the single-shot G_0W_0 approximation within the general plasmon pole model,[64] where the dielectric matrix energy cutoff is 10 Ry, and over 200 unoccupied bands are utilized for the summation. A coarse *k*-grid of 18 × 18 × 1 is used, which is further interpolated to a fine *k*-grid of 36 × 36 × 1 in order to obtain the electron−hole interaction kernel and solve the Bethe−Salpeter equation (BSE) for the excitonic effects and optical absorption spectra.[48]

ASSOCIATED CONTENT

Supporting Information

The Supporting Information is available free of charge at https://pubs.acs.org/doi/10.1021/acsaom.3c00389.

Projected density of states of AB1 bilayer *h*-BN and the single-particle carrier wave functions in the moiré superlattices (PDF)

AUTHOR INFORMATION

Corresponding Author

Li Yang − *Department of Physics, Washington University in St. Louis, St. Louis, Missouri 63130, United States; Institute of Materials Science and Engineering, Washington University in*

https://doi.org/10.1021/acsaom.3c00389
ACS Appl. Opt. Mater. 2024, 2, 166−172

St. Louis, St. Louis, Missouri 63130, United States; orcid.org/0000-0002-8611-6359; Email: lyang@physics.wustl.edu

Authors

Linghan Zhu − *Department of Physics, Washington University in St. Louis, St. Louis, Missouri 63130, United States;* orcid.org/0000-0002-9259-5077

Yizhou Wang − *Department of Physics, Washington University in St. Louis, St. Louis, Missouri 63130, United States*

Complete contact information is available at: https://pubs.acs.org/10.1021/acsaom.3c00389

Notes

The authors declare no competing financial interest.

■ ACKNOWLEDGMENTS

L.Z. and L.Y. are supported by the National Science Foundation (NSF) grant No. DMR-2124934. Y.W. is supported by the Air Force Office of Scientific Research (AFOSR) grant No. FA9550-20-1-0255. The simulation used Anvil at Purdue University through allocation DMR100005 from the Advanced Cyberinfrastructure Coordination Ecosystem: Services & Support (ACCESS) program, which is supported by National Science Foundation grants #2138259, #2138286, #2138307, #2137603, and #2138296.

■ REFERENCES

(1) Coe, S.; Woo, W.-K.; Bawendi, M.; Bulović, V. Electroluminescence from Single Monolayers of Nanocrystals in Molecular Organic Devices. *Nature* **2002**, *420* (6917), 800−803.
(2) Stouwdam, J. W.; Janssen, R. A. J. Red, Green, and Blue Quantum Dot LEDs with Solution Processable ZnO Nanocrystal Electron Injection Layers. *J. Mater. Chem.* **2008**, *18* (16), 1889−1894.
(3) Chuang, C.-H. M.; Brown, P. R.; Bulović, V.; Bawendi, M. G. Improved Performance and Stability in Quantum Dot Solar Cells through Band Alignment Engineering. *Nat. Mater.* **2014**, *13* (8), 796−801.
(4) Posthuma-Trumpie, G. A.; Wichers, J. H.; Koets, M.; Berendsen, L. B. J. M.; van Amerongen, A. Amorphous Carbon Nanoparticles: A Versatile Label for Rapid Diagnostic (Immuno)Assays. *Anal. Bioanal. Chem.* **2012**, *402* (2), 593−600.
(5) Li, H.; Liu, R.; Lian, S.; Liu, Y.; Huang, H.; Kang, Z. Near-Infrared Light Controlled Photocatalytic Activity of Carbon Quantum Dots for Highly Selective Oxidation Reaction. *Nanoscale* **2013**, *5* (8), 3289−3297.
(6) Li, Y.; Zhao, Y.; Cheng, H.; Hu, Y.; Shi, G.; Dai, L.; Qu, L. Nitrogen-Doped Graphene Quantum Dots with Oxygen-Rich Functional Groups. *J. Am. Chem. Soc.* **2012**, *134* (1), 15−18.
(7) Tran, K.; Moody, G.; Wu, F.; Lu, X.; Choi, J.; Kim, K.; Rai, A.; Sanchez, D. A.; Quan, J.; Singh, A.; Embley, J.; Zepeda, A.; Campbell, M.; Autry, T.; Taniguchi, T.; Watanabe, K.; Lu, N.; Banerjee, S. K.; Silverman, K. L.; Kim, S.; Tutuc, E.; Yang, L.; MacDonald, A. H.; Li, X. Evidence for Moiré Excitons in van Der Waals Heterostructures. *Nature* **2019**, *567* (7746), 71−75.
(8) Yu, H.; Liu, G. B.; Tang, J.; Xu, X.; Yao, W. Moiré Excitons: From Programmable Quantum Emitter Arrays to Spin-Orbit−Coupled Artificial Lattices. *Sci. Adv.* **2017**, *3* (11), No. e1701696.
(9) Lu, X.; Li, X.; Yang, L. Modulated Interlayer Exciton Properties in a Two-Dimensional Moiré Crystal. *Phys. Rev. B* **2019**, *100* (15), No. 155416.
(10) Baek, H.; Brotons-Gisbert, M.; Koong, Z. X.; Campbell, A.; Rambach, M.; Watanabe, K.; Taniguchi, T.; Gerardot, B. D. Highly Energy-Tunable Quantum Light from Moiré-Trapped Excitons. *Sci. Adv.* **2020**, *6* (37), No. eaba8526.
(11) Naik, M. H.; Kundu, S.; Maity, I.; Jain, M. Origin and Evolution of Ultraflat Bands in Twisted Bilayer Transition Metal Dichalcogenides: Realization of Triangular Quantum Dots. *Phys. Rev. B* **2020**, *102* (7), No. 075413.
(12) Zhao, H.; Zhu, L.; Li, X.; Chandrasekaran, V.; Baldwin, J. K.; Pettes, M. T.; Piryatinski, A.; Yang, L.; Htoon, H. Manipulating Interlayer Excitons for Ultra-Pure Near-Infrared Quantum Light Generation, arXiv:2205.02472. arXiv.org e-Print archive, 2022. https://doi.org/10.48550/arXiv.2205.02472.
(13) Mak, K. F.; Lee, C.; Hone, J.; Shan, J.; Heinz, T. F. Atomically Thin MoS2: A New Direct-Gap Semiconductor. *Phys. Rev. Lett.* **2010**, *105* (13), No. 136805.
(14) Kunstmann, J.; Mooshammer, F.; Nagler, P.; Chaves, A.; Stein, F.; Paradiso, N.; Plechinger, G.; Strunk, C.; Schüller, C.; Seifert, G.; Reichman, D. R.; Korn, T. Momentum-Space Indirect Interlayer Excitons in Transition-Metal Dichalcogenide van Der Waals Heterostructures. *Nat. Phys.* **2018**, *14* (8), 801−805.
(15) Xu, Y.; Liu, S.; Rhodes, D. A.; Watanabe, K.; Taniguchi, T.; Hone, J.; Elser, V.; Mak, K. F.; Shan, J. Correlated Insulating States at Fractional Fillings of Moiré Superlattices. *Nature* **2020**, *587* (7833), 214−218.
(16) Regan, E. C.; Wang, D.; Jin, C.; Utama, M. I. B.; Gao, B.; Wei, X.; Zhao, S.; Zhao, W.; Zhang, Z.; Yumigeta, K.; Blei, M.; Carlström, J. D.; Watanabe, K.; Taniguchi, T.; Tongay, S.; Crommie, M.; Zettl, A.; Wang, F. Mott and Generalized Wigner Crystal States in WSe2/WS2Moiré Superlattices. *Nature* **2020**, *579* (7799), 359−363.
(17) Li, H.; Li, S.; Regan, E. C.; Wang, D.; Zhao, W.; Kahn, S.; Yumigeta, K.; Blei, M.; Taniguchi, T.; Watanabe, K.; Tongay, S.; Zettl, A.; Crommie, M. F.; Wang, F. Imaging Two-Dimensional Generalized Wigner Crystals. *Nature* **2021**, *597* (7878), 650−654.
(18) Huang, X.; Wang, T.; Miao, S.; Wang, C.; Li, Z.; Lian, Z.; Taniguchi, T.; Watanabe, K.; Okamoto, S.; Xiao, D.; Shi, S. F.; Cui, Y. T. Correlated Insulating States at Fractional Fillings of the WS2/WSe2Moiré Lattice. *Nat. Phys.* **2021**, *17* (6), 715−719.
(19) Shabani, S.; Halbertal, D.; Wu, W.; Chen, M.; Liu, S.; Hone, J.; Yao, W.; Basov, D. N.; Zhu, X.; Pasupathy, A. N. Deep Moiré Potentials in Twisted Transition Metal Dichalcogenide Bilayers. *Nat. Phys.* **2021**, *17* (6), 720−725.
(20) Zhu, L.; Wang, H.; Yang, L. Moiré Potential Renormalization and Ultra-Flat Bands Induced by Quasiparticle-Plasmon Coupling. *npj Comput. Mater.* **2023**, *9* (1), No. 8.
(21) Klein, K.-F.; Gonschior, C. P.; Beer, D.; Eckhardt, H.-S.; Belz, M.; Shannon, J.; Khalilov, V.; Klein, M.; Jakob, C. *Silica-Based UV-Fibers for DUV Applications: Current Status*, SPIE Proceedings, Kalli, K.; Kanka, J.; Mendez, A., Eds.; SPIE, 2013.
(22) Matsumoto, T.; Tatsuno, I.; Hasegawa, T. Instantaneous Water Purification by Deep Ultraviolet Light in Water Waveguide: *Escherichia coli* Bacteria Disinfection. *Water* **2019**, *11* (5), No. 968.
(23) Kumamoto, Y.; Taguchi, A.; Smith, N. I.; Kawata, S. Deep Ultraviolet Resonant Raman Imaging of a Cell. *J. Biomed. Opt.* **2012**, *17* (7), No. 0760011.
(24) Mitra, S.; Aravindh, A.; Das, G.; Pak, Y.; Ajia, I.; Loganathan, K.; Di Fabrizio, E.; Roqan, I. S. High-Performance Solar-Blind Flexible Deep-UV Photodetectors Based on Quantum Dots Synthesized by Femtosecond-Laser Ablation. *Nano Energy* **2018**, *48*, 551−559.
(25) Sun, T.-P.; Huang, C.-T.; Lui, P.-W.; Chen, Y.-T.; Shieh, H.-L. *Novel Measurement System for Linear Array Type UVC Germicidal System*, IEEE Eurasia Conference on Biomedical Engineering, Healthcare and Sustainability (ECBIOS); IEEE, 2019; pp 57−60.
(26) Cassabois, G.; Valvin, P.; Gil, B. Hexagonal Boron Nitride Is an Indirect Bandgap Semiconductor. *Nat. Photonics* **2016**, *10* (4), 262−266.
(27) Xian, L.; Kennes, D. M.; Tancogne-Dejean, N.; Altarelli, M.; Rubio, A. Multiflat Bands and Strong Correlations in Twisted Bilayer Boron Nitride: Doping-Induced Correlated Insulator and Superconductor. *Nano Lett.* **2019**, *19* (8), 4934−4940.
(28) Su, C.; Zhang, F.; Kahn, S.; Shevitski, B.; Jiang, J.; Dai, C.; Ungar, A.; Park, J.-H.; Watanabe, K.; Taniguchi, T.; Kong, J.; Tang,

Z.; Zhang, W.; Wang, F.; Crommie, M.; Louie, S. G.; Aloni, S.; Zettl, A. Tuning Colour Centres at a Twisted Hexagonal Boron Nitride Interface. *Nat. Mater.* **2022**, *21* (8), 896−902.
(29) Bourrellier, R.; Amato, M.; Tizei, L. H. G.; Giorgetti, C.; Gloter, A.; Heggie, M. I.; March, K.; Stéphan, O.; Reining, L.; Kociak, M.; Zobelli, A. Nanometric Resolved Luminescence in H-BN Flakes: Excitons and Stacking Order. *ACS Photonics* **2014**, *1* (9), 857−862.
(30) Li, L.; Wu, M. Binary Compound Bilayer and Multilayer with Vertical Polarizations: Two-Dimensional Ferroelectrics, Multiferroics, and Nanogenerators. *ACS Nano* **2017**, *11* (6), 6382−6388.
(31) Yasuda, K.; Wang, X.; Watanabe, K.; Taniguchi, T.; Jarillo-Herrero, P. Stacking-Engineered Ferroelectricity in Bilayer Boron Nitride. *Science* **2021**, *372* (6549), 1458−1462.
(32) Kim, D. S.; Dominguez, R. C.; Mayorga-Luna, R.; Ye, D.; Embley, J.; Tan, T.; Ni, Y.; Liu, Z.; Ford, M.; Gao, F. Y.; Arash, S.; Watanabe, K.; Taniguchi, T.; Kim, S.; Shih, C. K.; Lai, K.; Yao, W.; Yang, L.; Li, X.; Miyahara, Y. Electrostatic Moiré Potential from Twisted Hexagonal Boron Nitride Layers. *Nat. Mater.* **2023**, 1−6, DOI: 10.1038/s41563-023-01637-7.
(33) Naik, M. H.; Jain, M. Ultraflatbands and Shear Solitons in Moiré Patterns of Twisted Bilayer Transition Metal Dichalcogenides. *Phys. Rev. Lett.* **2018**, *121* (26), No. 266401.
(34) Naik, M. H.; Regan, E. C.; Zhang, Z.; Chan, Y.-H.; Li, Z.; Wang, D.; Yoon, Y.; Ong, C. S.; Zhao, W.; Zhao, S.; Utama, M. I. B.; Gao, B.; Wei, X.; Sayyad, M.; Yumigeta, K.; Watanabe, K.; Taniguchi, T.; Tongay, S.; da Jornada, F. H.; Wang, F.; Louie, S. G. Intralayer Charge-Transfer Moiré Excitons in van Der Waals Superlattices. *Nature* **2022**, *609* (7925), 52−57.
(35) Plimpton, S. Fast Parallel Algorithms for Short-Range Molecular Dynamics. *J. Comput. Phys.* **1995**, *117* (1), 1−19.
(36) Maaravi, T.; Leven, I.; Azuri, I.; Kronik, L.; Hod, O. Interlayer Potential for Homogeneous Graphene and Hexagonal Boron Nitride Systems: Reparametrization for Many-Body Dispersion Effects. *J. Phys. Chem. C* **2017**, *121* (41), 22826−22835.
(37) Tersoff, J. New Empirical Approach for the Structure and Energy of Covalent Systems. *Phys. Rev. B* **1988**, *37* (12), 6991−7000.
(38) Zhong, X.; Yap, Y. K.; Pandey, R.; Karna, S. P. First-Principles Study of Strain-Induced Modulation of Energy Gaps of Graphene/BN and BN Bilayers. *Phys. Rev. B* **2011**, *83* (19), No. 193403.
(39) Cosma, D. A.; Wallbank, J. R.; Cheianov, V.; Fal, V. I. Moiré pattern as a magnifying glass for strain and dislocations in van der Waals heterostructures. *Faraday Discuss.* **2014**, 137−143.
(40) Wickramaratne, D.; Weston, L.; Van de Walle, C. G. Monolayer to Bulk Properties of Hexagonal Boron Nitride. *J. Phys. Chem. C* **2018**, *122* (44), 25524−25529.
(41) Mengle, K. A.; Kioupakis, E. Impact of the Stacking Sequence on the Bandgap and Luminescence Properties of Bulk, Bilayer, and Monolayer Hexagonal Boron Nitride. *APL Mater.* **2019**, *7* (2), No. 021106, DOI: 10.1063/1.5087836.
(42) Supporting Material.
(43) Wu, F.; Lovorn, T.; Macdonald, A. H. Topological Exciton Bands in Moiré Heterojunctions. *Phys. Rev. Lett.* **2017**, *118* (14), No. 147401.
(44) Feng, J.; Qian, X.; Huang, C. W.; Li, J. Strain-Engineered Artificial Atom as a Broad-Spectrum Solar Energy Funnel. *Nat. Photonics* **2012**, *6* (12), 866−872.
(45) He, K.; Poole, C.; Mak, K. F.; Shan, J. Experimental Demonstration of Continuous Electronic Structure Tuning via Strain in Atomically Thin MoS 2. *Nano Lett.* **2013**, *13* (6), 2931−2936.
(46) Song, W.; Yang, L. Quasiparticle Band Gaps and Optical Spectra of Strained Monolayer Transition-Metal Dichalcogenides. *Phys. Rev. B* **2017**, *96* (23), No. 235441.
(47) Cohen, M. L.; Louie, S. G.*Fundamentals of Condensed Matter Physics*; Cambridge University Press, 2016.
(48) Rohlfing, M.; Louie, S. G. Electron-Hole Excitations and Optical Spectra from First Principles. *Phys. Rev. B* **2000**, *62*, No. 4927.
(49) Zhu, L.; Yang, L. Quasiparticle Energies and Excitonic Effects of Chromium Trichloride: From Two Dimensions to Bulk. *Phys. Rev. B* **2020**, *101* (24), No. 245401.
(50) Sponza, L.; Amara, H.; Attaccalite, C.; Latil, S.; Galvani, T.; Paleari, F.; Wirtz, L.; Ducastelle, F. Direct and Indirect Excitons in Boron Nitride Polymorphs: A Story of Atomic Configuration and Electronic Correlation. *Phys. Rev. B* **2018**, *98* (12), No. 125206.
(51) Qiu, D. Y.; Da Jornada, F. H.; Louie, S. G. Optical Spectrum of MoS2: Many-Body Effects and Diversity of Exciton States. *Phys. Rev. Lett.* **2013**, *111* (21), No. 216805.
(52) Wu, F.; Lovorn, T.; Tutuc, E.; Macdonald, A. H. Hubbard Model Physics in Transition Metal Dichalcogenide Moiré Bands. *Phys. Rev. Lett.* **2018**, *121* (2), No. 026402.
(53) Javey, A.; Uddin, S. Z.; Kim, H.; Lorenzon, M.; Yeh, M.; Lien, D. H.; Barnard, E. S.; Htoon, H.; Weber-Bargioni, A. Neutral Exciton Diffusion in Monolayer MoS2. *ACS Nano* **2020**, *14* (10), 13433−13440.
(54) Rossi, A.; Zipfel, J.; Maity, I.; Lorenzon, M.; Francaviglia, L.; Regan, E. C.; Zhang, Z.; Nie, J. H.; Barnard, E.; Watanabe, K.; Taniguchi, T.; Rotenberg, E.; Wang, F.; Lischner, J.; Raja, A.; Weber-Bargioni, A. Phason-Mediated Interlayer Exciton Diffusion in WS2/WSe2Moir\'e Heterostructure, arXiv:2301.07750. arXiv.org e-Print archive, 2023. https://doi.org/10.48550/arXiv.2301.07750.
(55) Li, H.; Contryman, A. W.; Qian, X.; Ardakani, S. M.; Gong, Y.; Wang, X.; Weisse, J. M.; Lee, C. H.; Zhao, J.; Ajayan, P. M.; Li, J.; Manoharan, H. C.; Zheng, X. Optoelectronic Crystal of Artificial Atoms in Strain-Textured Molybdenum Disulphide. *Nat. Commun.* **2015**, *6* (1), No. 7381.
(56) Branny, A.; Kumar, S.; Proux, R.; Gerardot, B. D. Deterministic Strain-Induced Arrays of Quantum Emitters in a Two-Dimensional Semiconductor. *Nat. Commun.* **2017**, *8* (1), No. 15053.
(57) Zhao, H.; Zhu, L.; Li, X.; Chandrasekaran, V.; Baldwin, J. K.; Pettes, M. T.; Piryatinski, A.; Yang, L.; Htoon, H. Manipulating Interlayer Excitons for Near-Infrared Quantum Light Generation. *Nano Lett.* **2023**, *23*, 11006−11012, DOI: 10.1021/acs.nanolett.3c03296.
(58) Chen, P.; Yang, S.; Liu, F.; Han, C.; Hu, J.; Jiang, Y.; Chen, L. Nontoxic Blue-Emitting Hexagonal BN Quantum Dots for QLED Application Synthesized by Solvothermal Pyrolysis of Ammonia Borane. *Appl. Mater. Today* **2023**, *31*, No. 101744.
(59) Chen, P.; Yang, S.; Liu, F.; Jiang, Y.; Wang, Y.; Huang, Y.; Hu, J.; Chen, L. Blue-Emitting Orthorhombic Boron Nitride Quantum Dots and Quantum-Dot Light-Emitting Diodes. *Adv. Photonics Res.* **2023**, *4* (3), No. 2200344, DOI: 10.1002/adpr.202200344.
(60) Perdew, J. P.; Burke, K.; Ernzerhof, M. Generalized Gradient Approximation Made Simple. *Phys. Rev. Lett.* **1996**, *77*, No. 3865.
(61) Giannozzi, P.; Baroni, S.; Bonini, N.; Calandra, M.; Car, R.; Cavazzoni, C.; Ceresoli, D.; Chiarotti, G. L.; Cococcioni, M.; Dabo, I.; Dal Corso, A.; De Gironcoli, S.; Fabris, S.; Fratesi, G.; Gebauer, R.; Gerstmann, U.; Gougoussis, C.; Kokalj, A.; Lazzeri, M.; Martin-Samos, L.; Marzari, N.; Mauri, F.; Mazzarello, R.; Paolini, S.; Pasquarello, A.; Paulatto, L.; Sbraccia, C.; Scandolo, S.; Sclauzero, G.; Seitsonen, A. P.; Smogunov, A.; Umari, P.; Wentzcovitch, R. M. QUANTUM ESPRESSO: A Modular and Open-Source Software Project for Quantum Simulations of Materials. *J. Phys.: Condens. Matter* **2009**, *21* (39), No. 395502.
(62) Grimme, S.; Antony, J.; Ehrlich, S.; Krieg, H. A Consistent and Accurate Ab Initio Parametrization of Density Functional Dispersion Correction (DFT-D) for the 94 Elements H-Pu. *J. Chem. Phys.* **2010**, *132* (15), No. 154104, DOI: 10.1063/1.3382344.
(63) Deslippe, J.; Samsonidze, G.; Strubbe, D. A.; Jain, M.; Cohen, M. L.; Louie, S. G. BerkeleyGW: A Massively Parallel Computer Package for the Calculation of the Quasiparticle and Optical Properties of Materials and Nanostructures. *Comput. Phys. Commun.* **2012**, *183*, 1269−1289.
(64) Hybertsen, M. S.; Louie, S. G. Electron Correlation in Semiconductors and Insulators: Band Gaps and Quasiparticle Energies. *Phys. Rev. B* **1986**, *34*, No. 5390.